Engineering Structures 189 (2019) 48–61

Contents lists available at ScienceDirect

Engineering Structures

journal homepage: www.elsevier.com/locate/engstruct

Non-parametric shape design optimization of elastic-plastic shear panel dampers under cyclic loading

Jin-Xing Shi[a,b], Sho Kozono[c], Masatoshi Shimoda[a,*], Masahiro Takino[a], Daiki Wada[a], Yang Liu[d]

[a] Department of Advanced Science and Technology, Toyota Technological Institute, 2-12-1 Hisakata, Tempaku-ku, Nagoya, Aichi 468-8511, Japan
[b] Department of Production Systems Engineering and Sciences, Komatsu University, Nu-1-3 Shicyomachi, Komatsu, Ishikawa 923-8511, Japan
[c] Graduate School of Advanced Science and Technology, Toyota Technological Institute, 2-12-1 Hisakata, Tempaku-ku, Nagoya, Aichi 468-8511, Japan
[d] Department of Mechanical Engineering, Sojo University, 4-22-1 Ikeda, Nishi-ku, Kumamoto, Kumamoto 860-0082, Japan

ARTICLE INFO

Keywords:
Cyclic loading
Elastic-plastic
Large deformation
Non-parameter
Shape optimization
Shear panel damper

ABSTRACT

In this work, we develop a non-parametric shape optimization method for designing low yield steel shear panel dampers (SPDs) under cyclic loading to enhance their energy dissipation capacity and verify it by experiments. Considering material nonlinearity (elastic-plastic) and geometric nonlinearity (large deformation), we formulate a shape optimization problem based on the variational method for 3D solid continua under cyclic loading, in which the plastic work in terms of von Mises equivalent stress is used as the objective function under a volume constraint. Considering the optimality conditions for the plastic work maximization problem, we theoretically derive the shape gradient function based on the Lagrange multiplier method, the material derivative formula, and the adjoint variable method. The derived shape gradient function is used to the H^1 gradient method for designing the optimal shapes of 3D solid continua. We apply the developed shape optimization method to design SPDs made of low yield steel, which is an elastic-plastic material owning high-energy dissipation capacity. Cyclic enforced displacements acting on SPDs are used for simulating cyclic loading and evaluating the capacity of energy absorption of SPDs. To evaluate the nonlinear finite element analysis, we also perform cyclic loading test on SPDs. Two design examples of SPDs without and with holes are optimized to verify the validity of the developed shape optimization method. The results show that the developed optimization method works effectively to enhance the plastic work of SPDs. As a feature, this method can design SPDs more efficiently when considering the variation in the thickness direction.

1. Introduction

Utilizing the plastic deformation to absorb the seismic energy, shear panel dampers (SPDs) are one of the essential devices in infrastructures. For instance, SPDs can be assembled in bridge structures [1,2], such as between superstructure and bridge piers as shown in Fig. 1(a). They also can be set in steel structures as bracing type [1,3-5], e.g. X bracing type as shown in Fig. 1(b). In seismic design, many countries with high seismic activity adopt a two-level seismic design procedure, in which the earthquake ground motions are divided into minor to moderate earthquake for level 1 and large earthquake for level 2 [6]. To fit each of the two design levels, SPDs should be made of materials with inelastic excursions accompanied by large ductility, since the post-yielding hysteresis of the materials is the source of energy dissipation [7]. In the design of SPDs, identifying the cyclic loading induced by earthquake that generates shear response on the SPDs is also important, however, it is beyond the scope of the present work and we do not discuss it anymore.

Considering their excellent energy dissipation capacity under cyclic loading, low yield steel (LYS) SPDs have been widely applied for passive mitigation of seismic energy. Accordingly, scholars have been studied the yield strength and fatigue life of LYS SPDs [4,8–11]. Matteis et al. [4] carried out nonlinear dynamic analysis of steel frames enhanced with LYS SPDs to examine the seismic response, and concluded that LYS SPDs can strongly enhance the seismic behavior of steel frames. To utilize the ductility of LYS SPDs sufficiently, Zhang et al. [8] optimized the shapes of SPDs by introducing holes or ribs to alleviate the stress concentration, and conducted hysteretic incremental experiments to verify the improvement of the deformation capacity of the SPDs. For the same purpose of stress concentration reduction, Lee et al. [10] studied the cyclic behavior of steel strip dampers by introducing holes and evaluated it by cyclic loading test.

* Corresponding author.
E-mail address: shimoda@toyota-ti.ac.jp (M. Shimoda).

https://doi.org/10.1016/j.engstruct.2019.03.049
Received 2 October 2018; Received in revised form 1 March 2019; Accepted 16 March 2019

Nomenclature

$(\bar{\cdot})$	variation
$(\cdot)'$	shape derivative
$(\dot{\cdot})(=(\cdot)' + (\cdot)_{,i}V_i)$	material derivative
$(\cdot)_{,i}(=\partial(\cdot)/\partial x_i)$	partial differential notation
$(\hat{\cdot})$	the correction term
$a(\cdot,\cdot)$	internal virtual work
C_{ijkl}	elastic-plastic stiffness tensor
D	feasible set of $T_s(\Omega)$
E	Young's modulus
$\boldsymbol{G}$ $(=G\boldsymbol{n})$	shape gradient function
$\boldsymbol{h}(\boldsymbol{X})$ $(=h_k(\boldsymbol{X}))$	enforced displacement vector
$l(\cdot)$	external virtual work
$l_{,t}(\cdot)$	virtual work rate of external load
$l_{h,t}(\cdot)$	virtual work rate of enforced displacements
L	Lagrange functional
M	volume
M_0	constraint volume
N_i	designated points
$\boldsymbol{P}(\boldsymbol{X}, t)$ $(=P_i(\boldsymbol{X}, t))$	external load vector
s	iteration history of domain variation
t, τ	time
T	final time
$T_s(\boldsymbol{X})$	one-to-one mapping of domain
U	kinematically admissible set of displacement
U_0	kinematically admissible set of displacement variation or adjoint displacement
$\boldsymbol{u} = \{u_i\}$	displacement vector
$\bar{\boldsymbol{u}} = \{\bar{u}_i\}$	adjoint displacement vector
$\boldsymbol{V}$	design velocity field
W	plastic work
$\boldsymbol{x}(=\{x_1, x_2, x_3\})$	position vector in Ω_s
$\boldsymbol{X}(=\{X_1, X_2, X_3\})$	position vector in Ω
$\mathbb{R}$	a set of real numbers
$\mathbb{R}^3$	3-dimensional space
$\delta\varepsilon^{pl}(t)$	variation of plastic strain
$\varepsilon_{ij}(\boldsymbol{u})$	strain tensor
$\hat{\varepsilon}_{ij}(\boldsymbol{u})$	correction term with respect to adjoint strain
$\varepsilon^{pl}(t)$	plastic strain
ν	Poisson's ratio
$\boldsymbol{\sigma}(\boldsymbol{u})(=\sigma_{ij}(\boldsymbol{u}))$	stress tensor
$\sigma_{Mises}(t)$	von Mises equivalent stress
Δt	time variation
Γ	boundary of the initial domain Ω
Γ_s	boundary of domain after domain variation Ω_s
Λ	Lagrange multiplier for volume constraint
Ω	domain of the initial solid continuum
Ω_s	domain of the solid continuum after domain variation

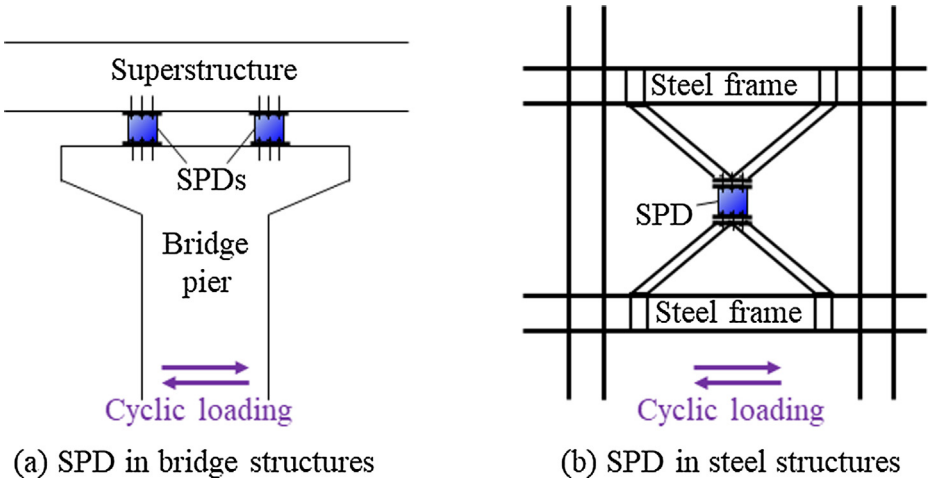

Fig. 1. Schematic diagram of SPDs assembled in full-scale structures.

On the other hand, finite element method (FEM)-based parametric shape optimization method for designing SPDs makes an important role for enhancing their energy dissipation capacity under cyclic loading [12]. There are two nonlinearities in finite element analysis of SPDs, which are geometric nonlinearity and material nonlinearity. Geometric nonlinearity relates to nonlinear strain-displacement relations and can lead to a large deformation problem. Material nonlinearity is due to nonlinear constitutive behavior of the material, in which a widely used approach is to treat the material as an elastic-plastic strain hardening material and perform an incremental analysis [13]. Hibbitt et al. [14] reviewed the nonlinear finite element analysis works regarding to large deformation and material nonlinearity at the time and firstly developed an incremental and piecewise FEM for large deformation reference to the elastic-plastic materials. The motivation of this study is to develop a FEM-based non-parametric shape optimization method for designing the elastic-plastic SPDs (without or with holes) under cyclic loading considering geometric nonlinearity and material nonlinearity.

Large deformation problem, in terms of geometric nonlinearity, demands methods to estimate the yield strength or fatigue life of engineering components and structures under cyclic loading [15–22]. For example, Döring et al. [15] proposed an improved set of constitutive equations for estimating the fatigue life of a thin-walled tubular specimen under cyclic loading, and compared the results to the experimental results. Usami et al. [18] conducted low-cycle fatigue (LCF) test to address the LCF strength of aluminum alloys in order to enhance the durability of buckling-restrained braces utilized in bridge engineering. Considering geometric nonlinearity, Ihara et al. [23] proposed a shape optimization method for designing 3D solid continua in the displacement path control problem. With respect to large deformation problem, small strain formulation can be taken as a special case of nonlinear large strain formulation [14]. Kosaka et al. [24] carried out shape design optimization of shell structures in plastic range for the reaction forces control problem, in which the Green–Lagrange strain and the second Piola–Kirchhoff stress were adopted to deal with large deformation in the structural analysis.

Shape design optimization is a procedure to improve or enhance the

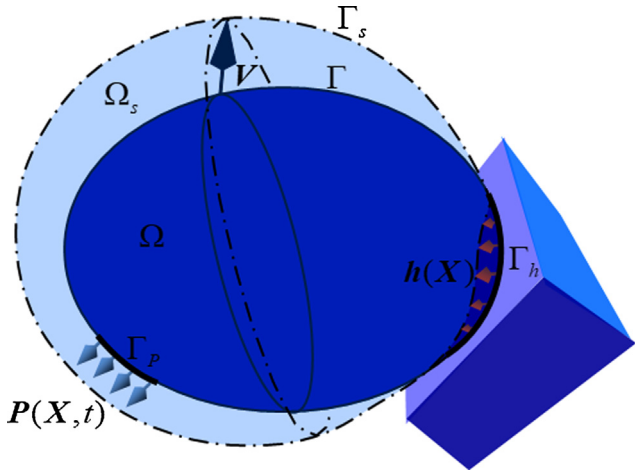

Fig. 2. Schematic diagram of domain variation in the solid continuum.

performance of structures (e.g. SPDs) by optimizing design parameters, and the shape optimization methods can be generally classified into parametric method and non-parametric method. The parametric method based on basis vectors is effective for reducing the number of design variables, but needs considerable knowledge and experience of shape parameterization among designers [12,25–30]. In contrast, the non-parametric method for obtaining free-form optimal shapes is a parameter-free optimization method, which has advantages of treating large-scale problems efficiently and owning the ability to obtain optimal shapes without design parameter [31–36]. Meske et al. [31] proposed a new shape optimization method for continuum solids based on an optimality criterion, where the non-parametric geometry representation resulted in a complete design space for the FEM-based optimization, and hence was preferable to any restricted design space. Le et al. [32] proposed a gradient-based non-parametric optimization method that used finite element node coordinates as design variables that allowed the most freedom for shape change and avoided the time-consuming parametric optimization process.

The traction method, also named the H^1 gradient method, is a one of the non-parametric shape optimization method, which consists of sensitivity analysis, derivation of shape gradient function and a gradient method with a P. D. E. (Partial Differential Equation) smoother in the Hilbert space for shape optimization of continua. This method was firstly proposed by Azegami [37] and some related works have been reported for linear elastic problems of 3D continua [38–40]. The traction method is a non-parameter shape optimization method that treats all nodes in the body as design variables. The advantages of this method include efficiency for treating large-scale problems and the ability to obtain smooth free-form optimal shapes of 3D solid continua (e.g. SPDs).

Most of the referred shape optimization works above focus on designing linear elastic materials. Because SPDs are usually made of LYS, an elastic-plastic material owning high LCF behavior under cyclic loading, material nonlinearity (e.g., elastic-plastic property) needs to be considered in shape design optimization of SPDs. However, FEM-based shape optimization for elastic-plastic materials is complicated and requires huge computation time. Hence, shape optimization for elastic-plastic materials was seldom carried out [24,28,29,41–43]. Ihara et al. [42] presented a non-parametric shape design optimization of 3D solid continua taking into account elastic-plastic property for minimizing the external work. Deng et al. [28,29] optimized the shapes of steel SPDs and U-shaped damper made of elastic-plastic materials using the parametric optimization method, where they carried out finite element analysis using ABAQUS, and verified the numerical results by cyclic loading test. Anyway, FEM-based numerical analysis of SPDs considering large deformation and material nonlinearity needs some

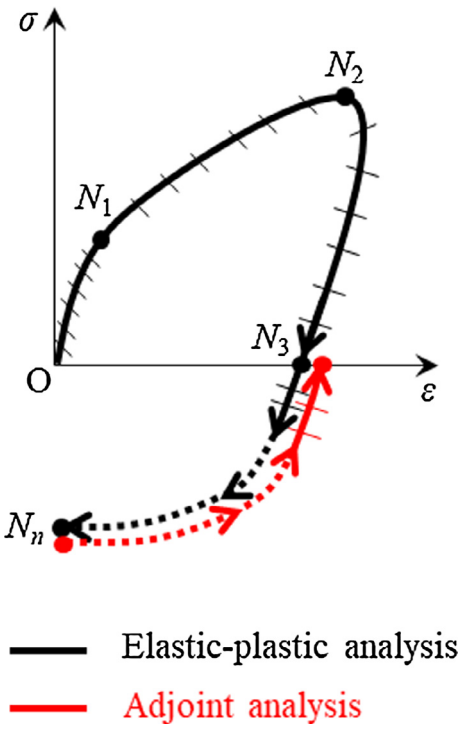

Fig. 3. Schematic diagram of elastic-plastic analysis and adjoint analysis.

assumptions, thus experimental verification is preferred. Accordingly, we also conduct experimental works to verify the proposed method with nonlinear finite element analysis in the present work.

Considering both geometric nonlinearity and material nonlinearity, we extend the traction method for shape design optimization of elastic-plastic SPDs under cyclic loading, and conduct the cyclic loading test on SPDs for experimental verification. In Section 2, we introduce the basic concepts of shape optimization method for 3D solid continua considering both geometric nonlinearity and material nonlinearity. In Section 3, we develop the non-parametric shape optimization method for designing elastic-plastic SPDs under cyclic loading and construct the shape optimization system. In Section 4, we present the experimental work of the cyclic loading test on LYS SPDs. In Section 5, we optimize two examples of SPDs without or with holes to verify the validity of the developed shape optimization method and express the comparison results between nonlinear finite element analysis and experiments. Finally, remarkable conclusions are presented in Section 6.

2. Basic concepts of shape design optimization of shear panel dampers

2.1. Domain variation in 3D solid continua

To develop the non-parametric shape optimization method for designing SPDs, we introduce the domain variation in 3D solid continua based on the shape gradient method at first. As shown in Fig. 2, a 3D solid continuum owns the initial domain $\Omega \subset \mathbb{R}^3$ and its boundary Γ. This solid continuum undergoes variation (i.e. the design velocity field) $\boldsymbol{V}$, so that the initial domain and boundary become Ω_s and Γ_s, respectively. The domain variation of the 3D solid continuum can be expressed by a one-to-one mapping, given as:

$$T_s(\boldsymbol{X}): \boldsymbol{X} \in \Omega \mapsto \boldsymbol{x} \in \Omega_s, \quad s \geqslant 0 \tag{1}$$

The design velocity field $\boldsymbol{V}$ for shape design optimization is given as a derivative of $T_s(\boldsymbol{X})$ in terms of s, shown as:

$$\boldsymbol{V}(\boldsymbol{X}) = \frac{\partial T_s}{\partial s}(T_s^{-1}(\boldsymbol{X})) \tag{2}$$

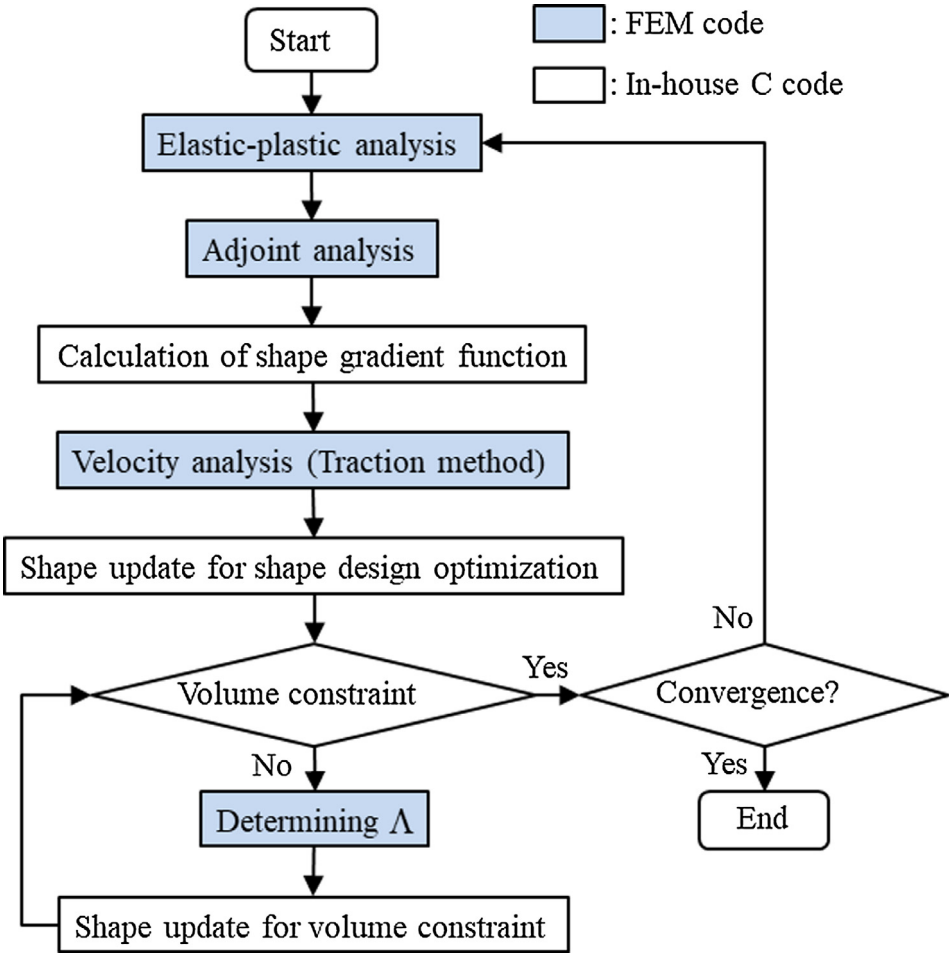

Fig. 4. Flowchart of the non-parametric shape optimization system.

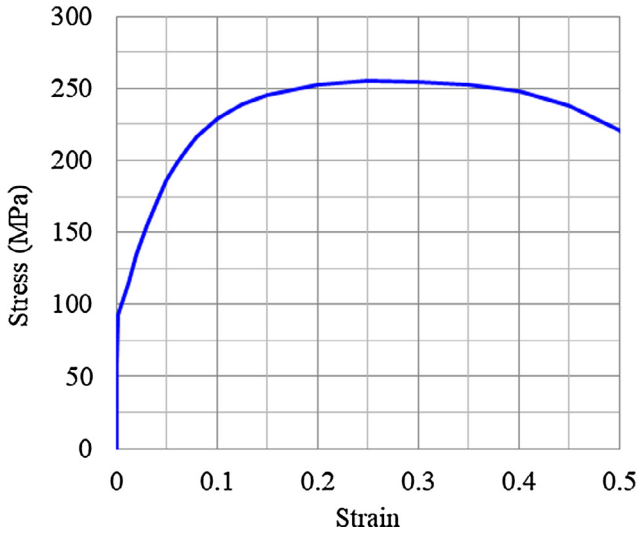

Fig. 5. Constitutive law of LY100.

The determination of $\boldsymbol{V}$ is a key point for shape updating in the shape design optimization, which is named velocity analysis or sensitivity analysis that has been introduced in detail in our previous works [39,40]. We will derive the shape gradient function for determining the optimal design velocity field in Section 3.2.

2.2. Weak-form governing equation considering geometric and material nonlinearities

According to geometric nonlinearity, we assume a large displacement and small strain formulation as a special case of the nonlinear large strain formulation [14], and adopt the small strain for simplicity in the present work. The strain rate tensor of 3D solid continua is shown as:

$$\varepsilon_{ij,t}(\boldsymbol{u}_{,t}) = \frac{1}{2}(u_{i,jt} + u_{j,it}) \tag{3}$$

Then, we consider material nonlinearity in the constitutive equation, in which a relationship between the stress rate tensor and the strain rate tensor is set based on the classical elastic-plastic theory for simplicity, shown as:

$$\sigma_{ij,t}(t) = C_{ijkl}(\boldsymbol{\sigma}(t))\varepsilon_{kl,t}(t) \tag{4}$$

where C_{ijkl} is a function of $\boldsymbol{\sigma}(t)$ in the elastic-plastic constitutive equation. Thus, based on the principle of virtual displacements, the weak-form governing equation in incremental form within $t \in (0, T)$ of a 3D solid continuum under external load and enforced displacement can be derived as:

$$\int_0^T \{l_{,t}(\bar{\boldsymbol{u}}) - a(\boldsymbol{u}_{,t}, \bar{\boldsymbol{u}})\}dt = 0, \quad \boldsymbol{u} \in U, \quad \forall\, \bar{\boldsymbol{u}} \in U_0 \tag{5}$$

where

$$l_{,t}(\bar{\boldsymbol{u}}) = \int_{\Gamma_s} P_{i,t}\bar{u}_i d\Gamma \tag{6}$$

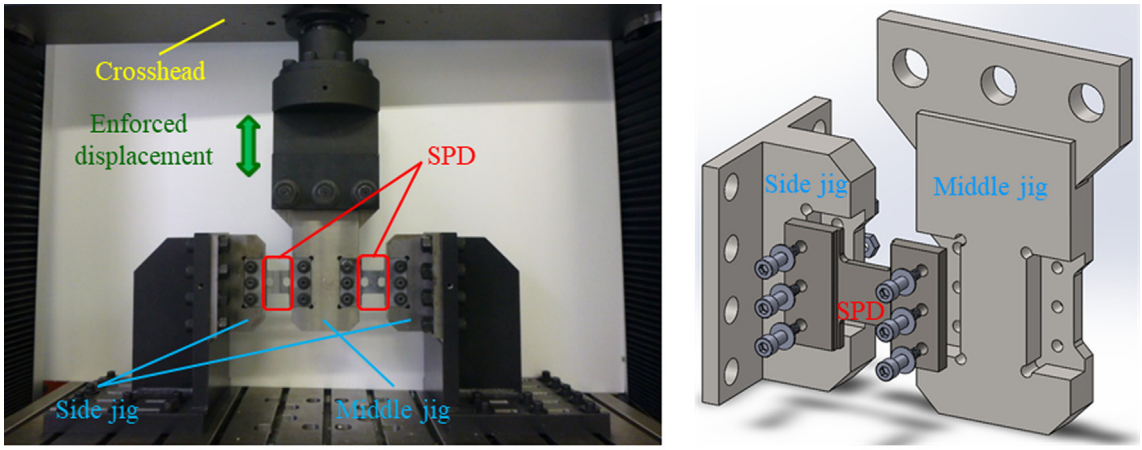

Fig. 6. Cyclic loading test setup.

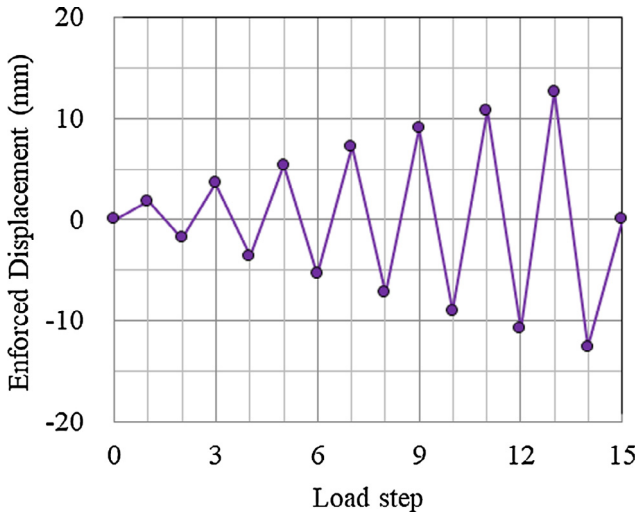

Fig. 7. Enforced displacement history of cyclic loading test.

$$l_{h,t}(\tilde{\boldsymbol{u}}) = \int_{\Omega_s} C_{ijkl} h_{k,lt} \bar{u}_{i,j} dx \tag{7}$$

$$a(\boldsymbol{u}_{,t}, \tilde{\boldsymbol{u}}) = \int_{\Omega_s} C_{ijkl}(\boldsymbol{\sigma}) \varepsilon_{kl,t}(\boldsymbol{u}_{,t}) \bar{\varepsilon}_{ij}(\tilde{\boldsymbol{u}}) dx = \int_{\Omega_s} C_{ijkl} u_{k,lt} \bar{u}_{i,j} dx \tag{8}$$

$$U = \{\boldsymbol{u}(\cdot,\cdot) \in (\mathrm{H}^1(\Omega_s \times (0, T)))^n \} | (u_i n_{ri})|_{x\in\Gamma} = 0, \quad r = 1, 2, \cdots, n, \quad \boldsymbol{u}|_{t=0} = \mathbf{0}\} \tag{9}$$

$$U_0 = \{\tilde{\boldsymbol{u}}(\cdot,\cdot) \in (\mathrm{H}^1(\Omega_s \times (0, T)))^n \} | (u_i n_{ri})|_{x\in\Gamma} = 0, \quad r = 1, 2, \cdots, n\} \tag{10}$$

where $(\mathrm{H}^1(\Omega_s \times (0, T)))^n$ denotes the Hilbert space of order 1 on the domain $\Omega_s \times (0, T)$ that consists of n-dimensional vector functions.

3. Non-parametric shape optimization method for designing shear panel dampers

3.1. Plastic work maximization problem

The von Mises yield criterion, a formula for combining three principal stress into an equivalent stress, has been widely used in materials science and engineering [44–46]. In the present work, we develop a non-parametric shape optimization method for elastic-plastic 3D solid

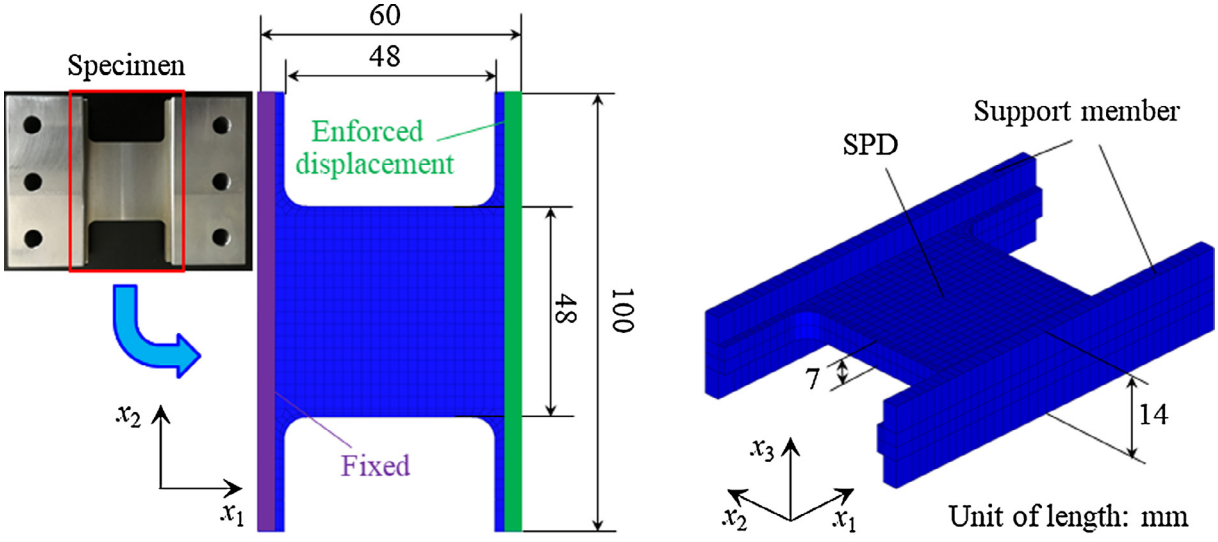

Fig. 8. Initial shape of example 1.

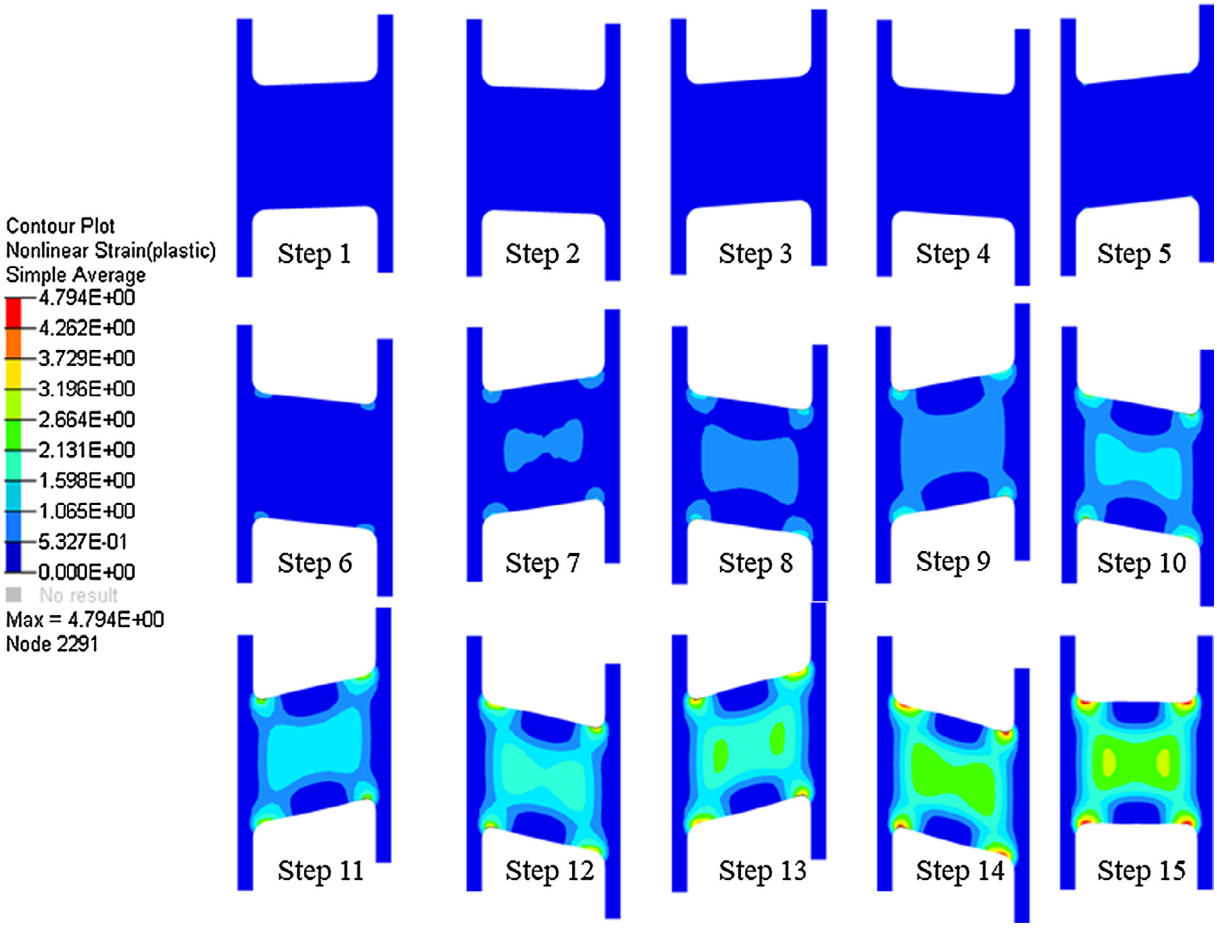

Fig. 9. Contour maps of plastic strain distribution in the initial shape of example 1 at each load step.

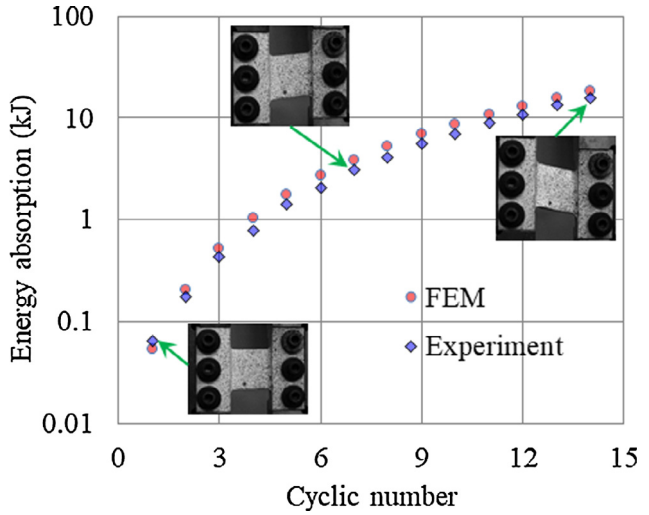

Fig. 10. Numerical vs. Experimental results of energy absorption of initial shape of Example 1.

continua (e.g. SPDs) under cyclic loading, in which the plastic work in terms of von Mises stress is used as the objective function, given as:

$$W = \int_{\Omega_s} \sigma_{Mises}(t)\delta\varepsilon^{pl}(t)dx = \int_{\Gamma_s} P_i u_{i,t} d\Gamma \tag{11}$$

Thereby, the plastic work maximization problem is formulated as:

Given Ω (12)

find $\boldsymbol{V}$ (13)

that minimizes $-W$ (14)

subject to Eq. (5) and $M \leqslant M_0$ (15)

In the next section, we will derive the shape gradient function for determining the design velocity field $\boldsymbol{V}$ utilized in velocity analysis.

3.2. Derivation of shape gradient function

We use the Lagrange multiplier method and the material derivative formula for the shape design optimization of SPDs in the plastic work maximization problem. As expressed in Nomenclature, material derivative is defined as $(\dot{\bullet}) = (\bullet)' + (\bullet)_{,i}V_i$, where $(\bullet)'$ indicates shape derivative (i.e. the partial derivative with respect to t) and $(\bullet)_{,i}V_i$ is the convective term [47]. Considering the objective function (Eq. (11)), the governing equation (Eq. (5)) and the volume constraint (Eq. (15)), the Lagrange functional L for this problem can be written as:

$$L = \int_0^T \{-W + l_{,t}(\tilde{\boldsymbol{u}}) - a(\boldsymbol{u}_{,t}, \tilde{\boldsymbol{u}})\}dt + \Lambda(M - M_0) \tag{16}$$

The material derivative of L with respect to the domain variation is derived using the design velocity field $\boldsymbol{V}$ as:

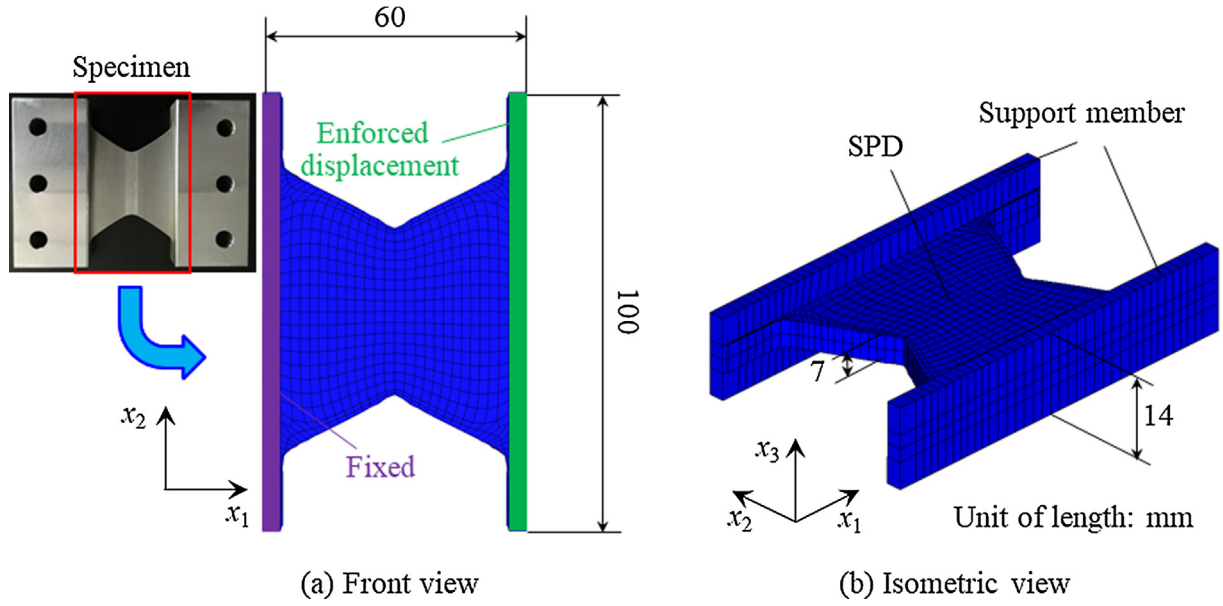

Fig. 11. Optimal shape of example 1 without thickness variation.

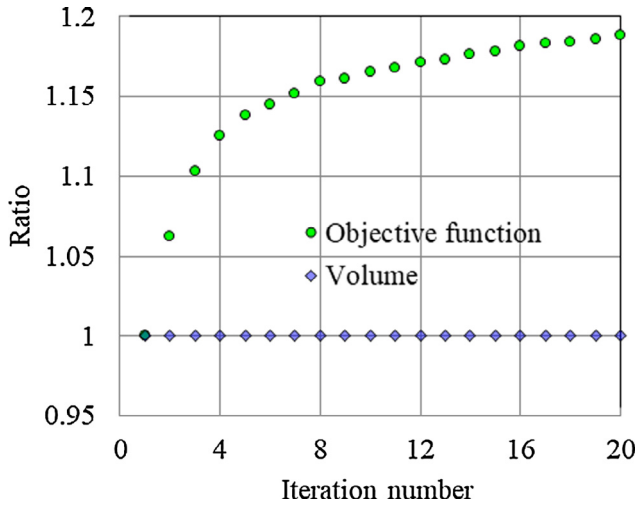

Fig. 12. Iteration history of example 1 without thickness variation.

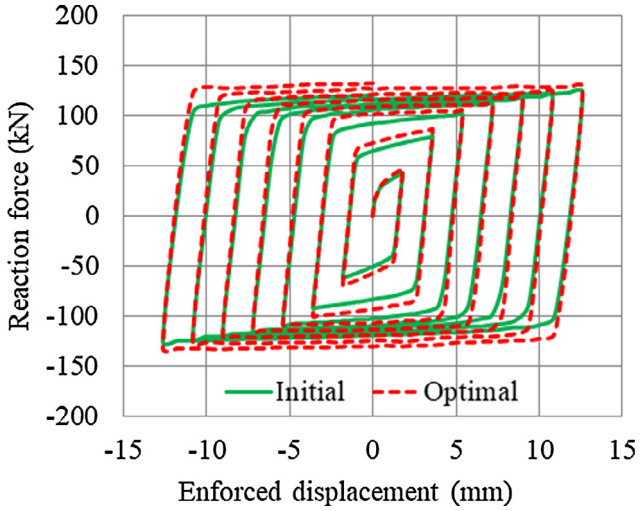

Fig. 13. Comparison of reaction force-enforced displacement curves of initial shape and optimal shape of example 1 without thickness variation.

$$\begin{aligned}\dot{L} = &-W' + \int_0^T [\int_{\Gamma_s} \{P'_{i,t}\bar{u}_i + P_{i,t}\bar{u}'_i + (P_{i,jt}n_j\bar{u}_i + P_{i,t}\bar{u}_{i,j}n_j \\ &+ P_{i,t}\bar{u}_i\kappa)n_k V_k\}d\Gamma \\ &- \int_{\Omega_s}(C'_{ijkl}h_{k,lt}\bar{u}_{i,j} + C_{ijkl}h'_{k,lt}\bar{u}_{i,j} + C_{ijkl}h_{k,lt}\bar{u}'_{k,l})dx \\ &- \int_{\Gamma_s} C_{ijkl}h_{k,lt}\bar{u}_{i,j}n_m V_m d\Gamma \\ &- \int_{\Omega_s}(C'_{ijkl}u_{k,lt}\bar{u}_{i,j} + C_{ijkl}u'_{k,lt}\bar{u}_{i,j} + C_{ijkl}u_{k,lt}\bar{u}'_{k,l})dx \\ &- \int_{\Gamma_s} C_{ijkl}u_{k,lt}\bar{u}_{i,j}n_m V_m d\Gamma]dt \\ &+ \dot{\Lambda}(M - M_0) + \int_{\Gamma_s}\Lambda n_i V_i d\Gamma \\ = &\int_0^T [\{l_{,t}(\bar{\boldsymbol{u}}') - l_{h,t}(\bar{\boldsymbol{u}}') - a(\boldsymbol{u}_{,t}, \bar{\boldsymbol{u}}')\} + \{-l(\boldsymbol{u}'_{,t}) + l_h(\boldsymbol{u}'_{,t}) - a(\boldsymbol{u}'_{,t}, \bar{\boldsymbol{u}}') \\ &- a_C(\{\boldsymbol{u}'_{,t}\}_0^T, \boldsymbol{u}_{,t}, \bar{\boldsymbol{u}}') - a_C(\{\boldsymbol{h}'_{,t}\}_0^T, \boldsymbol{h}_{,t}, \bar{\boldsymbol{u}})\}]dt + \dot{\Lambda}(M - M_0) + \langle G\boldsymbol{n}, \boldsymbol{V}\rangle \end{aligned} \tag{17}$$

where $\{\ \}_0^T$ indicates time integral from 0 to T. $a_C(\{\boldsymbol{u}'_{,t}\}_0^T, \boldsymbol{u}_{,t}, \bar{\boldsymbol{u}})$ and $a_C(\{\boldsymbol{h}'_{,t}\}_0^T, \boldsymbol{h}_{,t}, \bar{\boldsymbol{u}})$ are the terms with respect to the stiffness variation of elastic-plastic SPDs according to the adjoint displacement during the cyclic loading and the enforced displacement [23], respectively, shown as:

$$a_C(\{\boldsymbol{u}'_{,t}\}_0^T, \boldsymbol{u}_{,t}, \bar{\boldsymbol{u}}) = \int_{\Omega_s} C'_{ijkl}u_{k,lt}\bar{u}_{i,j}dx \tag{18}$$

$$a_C(\{\boldsymbol{h}'_{,t}\}_0^T, \boldsymbol{h}_{,t}, \bar{\boldsymbol{u}}) = \int_{\Omega_s} C'_{ijkl}h_{k,lt}\bar{u}_{i,j}dx \tag{19}$$

Note that due to difficulty of solving C'_{ijkl}, $a_C(\{\boldsymbol{u}'_{,t}\}_0^T, \boldsymbol{u}_{,t}, \bar{\boldsymbol{u}})\}$ and $a_C(\{\boldsymbol{h}'_{,t}\}_0^T, \boldsymbol{h}_{,t}, \bar{\boldsymbol{u}})$ should be calculated by a special method as shown in the next section.

The optimality conditions of Eq. (17) are given as:

$$\int_0^T \{l_{,t}(\bar{\boldsymbol{u}}') - a(\boldsymbol{u}_{,t}, \bar{\boldsymbol{u}}')\}dt = 0, \quad \forall\ \bar{\boldsymbol{u}}' \in U_0 \tag{20}$$

$$\int_0^T \{l(\boldsymbol{u}'_{,t}) - a(\boldsymbol{u}'_{,t}, \bar{\boldsymbol{u}}) - a_C(\{\boldsymbol{u}'_{,t}\}_0^T, \boldsymbol{u}_{,t}, \bar{\boldsymbol{u}}) - a_C(\{\boldsymbol{h}'_{,t}\}_0^T, \boldsymbol{h}_{,t}, \bar{\boldsymbol{u}})\}dt = 0, \quad \forall\ \boldsymbol{u}' \in U \tag{21}$$

$$\Lambda \geqslant 0, \quad M - M_0 \leqslant 0, \quad \Lambda(M - M_0) = 0 \tag{22}$$

where Eq. (20) is the governing equation of elastic-plastic analysis, Eq. (21) is the adjoint equation for the adjoint displacement $\bar{\boldsymbol{u}}$ in adjoint analysis, and Eq. (22) is in terms of the volume constraint. Assuming that the external loads $\boldsymbol{P}(\boldsymbol{X}, t)$ is not varied in the design space and time (i.e. $\boldsymbol{P}' = \dot{\boldsymbol{P}} = 0$) and the enforced displacement direction is conserved

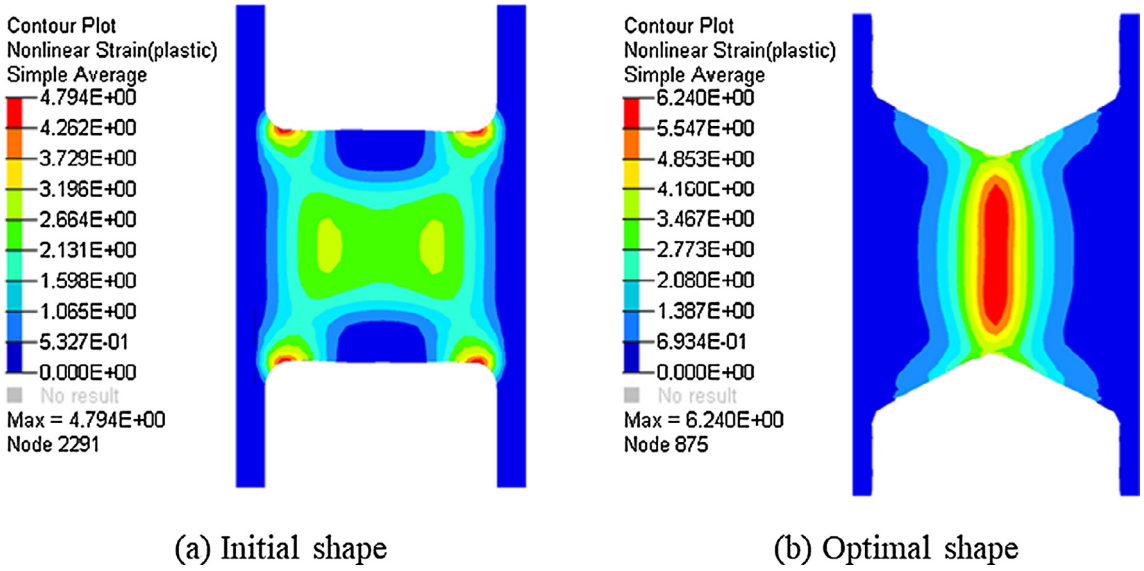

Fig. 14. Contour maps of plastic strain distribution in the SPDs of example 1 at the last cyclic step.

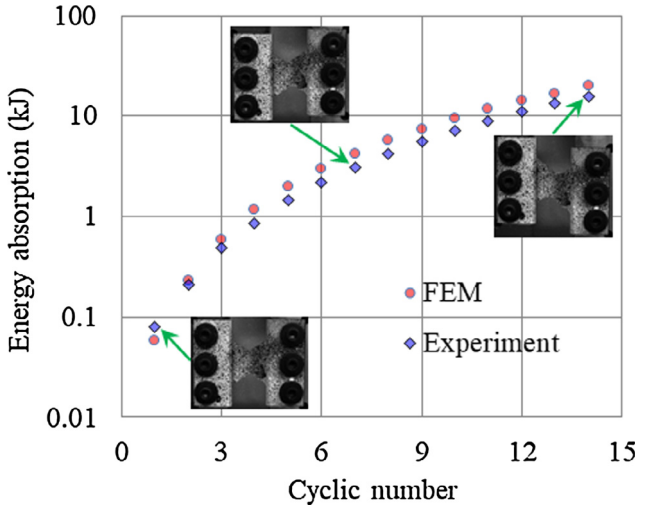

Fig. 15. Numerical vs. Experimental results of energy absorption of optimal shape of Example 1 without thickness variation.

(i.e. $\boldsymbol{h}' = \dot{\boldsymbol{h}} = 0$), the material derivative can be obtained as:

$$\dot{L} = \langle G\boldsymbol{n},\ \boldsymbol{V}\rangle = \int_0^T \{\int_{\Gamma_s} (C_{ijkl}u_{k,lt}\bar{u}_{i,j} + C_{ijkl}h_{k,lt}\bar{u}_{i,j} + \Lambda)n_m V_m d\Gamma\}dt \tag{23}$$

3.3. Solution of the adjoint equation

Eq. (20) can be solved using a general nonlinear FEM, whereas the solution of Eq. (21) is too complicated to be solved due to the terms of $a_C(\{\boldsymbol{u}'_{,t}\}_0^T, \boldsymbol{u}_{,t}, \bar{\boldsymbol{u}})\}$ and $a_C(\{\boldsymbol{h}'_{,t}\}_0^T, \boldsymbol{h}_{,t}, \bar{\boldsymbol{u}})$. Ihara et al. [42] proposed a solution method for the adjoint equation based on the path dependency of $\boldsymbol{\sigma}(t)$ within $0 \leqslant \tau < t \leqslant T$ with respect to the monotonic increasing loading. Here, we extend this method to solve the adjoint equation according to the cyclic loading and the enforced displacement. Because the method of solving $a_C(\{\boldsymbol{u}'_{,t}\}_0^T, \boldsymbol{u}_{,t}, \bar{\boldsymbol{u}})\}$ and $a_C(\{\boldsymbol{h}'_{,t}\}_0^T, \boldsymbol{h}_{,t}, \bar{\boldsymbol{u}})$ are the same, the solution of $a_C(\{\boldsymbol{u}'_{,t}\}_0^T, \boldsymbol{u}_{,t}, \bar{\boldsymbol{u}})\}$ is expressed as a representative. We rewrite $a_C(\{\boldsymbol{u}'_{,t}\}_0^T, \boldsymbol{u}_{,t}, \bar{\boldsymbol{u}})\}$ as:

$$\begin{aligned} a_C(\{\boldsymbol{u}'_{,t}\}_0^T, \boldsymbol{u}_{,t}, \bar{\boldsymbol{u}})\} &= \int_{\Omega_s} C'_{ijkl}u_{k,lt}\bar{u}_{i,j}dx = \int_{\Omega_s} \frac{\partial C_{ijkl}}{\partial \sigma_{mn}}\sigma'_{mn}u_{k,lt}\bar{u}_{i,j}dx \\ &= \int_{\Omega_s} \frac{\partial C_{ijkl}}{\partial \sigma_{mn}}\left(\int_0^t \frac{\partial \sigma_{mn}(t)}{\partial \sigma_{op}(\tau)}\frac{\partial \sigma_{op,t}(\sigma)}{\partial \varepsilon_{qr}(\boldsymbol{u}_{,t}(\sigma))}u'_{q,rt}(\tau)d\tau\right)u_{k,lt}\bar{u}_{i,j}dx \\ &= \int_{\Omega_s} \frac{\partial C_{ijkl}}{\partial \sigma_{mn}}\left(\int_0^t \frac{\partial \sigma_{mn}(t)}{\partial \sigma_{op}(\tau)}C_{opqr}(\tau)u'_{q,rt}(\tau)d\tau\right)u_{k,lt}\bar{u}_{i,j}dx \end{aligned} \tag{24}$$

Considering the path dependency, $\boldsymbol{\sigma}(t)$ can be obtained within $0 \leqslant \tau < t \leqslant T$ where $\partial\sigma_{ij}(t)/\partial\sigma_{kl}(\tau)$ is defined as:

$$\frac{\partial \sigma_{ij}(t)}{\partial \sigma_{kl}(\tau)} \equiv \lim_{\Delta t \to 0} \frac{\partial \sigma_{ij}(t)}{\partial \sigma_{mn}(t-\Delta t)}\frac{\partial \sigma_{mn}(t-\Delta t)}{\partial \sigma_{op}(t-2\Delta t)} \times \cdots \frac{\partial \sigma_{op}(\tau+\Delta t)}{\partial \sigma_{kl}(\tau)} \tag{25}$$

Using the Dirichlet's theorem for double integral of a given continuum function $\phi(t, \tau)$, which is assumed to be continuous in $0 \leqslant \tau < t \leqslant T$, shown as:

$$\int_0^T \int_0^t \phi(t, \tau)d\tau dt = \int_0^T \int_\tau^T \phi(t, \tau)dtd\tau \tag{26}$$

Then, we have

$$\begin{aligned} &\int_0^T a_C(\{\boldsymbol{u}'_{,t}\}_0^T, \boldsymbol{u}_{,t}, \bar{\boldsymbol{u}})\}dt \\ &= \int_{\Omega_s}\int_0^T\int_0^t \frac{\partial C_{ijkl}(t)}{\partial \sigma_{mn}(t)}\frac{\partial \sigma_{mn}(t)}{\partial \sigma_{op}(\tau)}C_{opqr}(\tau)u_{k,lt}\bar{u}_{i,j}u'_{q,rt}d\tau dtdx \\ &= \int_{\Omega_s}\int_0^T\int_\tau^T \frac{\partial C_{ijkl}(t)}{\partial \sigma_{mn}(t)}\frac{\partial \sigma_{mn}(t)}{\partial \sigma_{op}(\tau)}C_{opqr}(\tau)u_{k,lt}\bar{u}_{i,j}u'_{q,rt}dtd\tau dx \\ &= \int_0^T a(\boldsymbol{u}'_{,t}(\tau), \hat{\bar{\boldsymbol{u}}}(\tau))d\tau \end{aligned} \tag{27}$$

where the correction term with respect to the adjoint displacement variation $\hat{\bar{\boldsymbol{u}}}(\tau)$ can be expressed by the strain component $\hat{\varepsilon}_{op}(\hat{\bar{\boldsymbol{u}}}(\tau))$, given as [42]:

$$\hat{\varepsilon}_{op}(\hat{\bar{\boldsymbol{u}}}(\tau)) = \int_\tau^T \frac{\partial C_{ijkl}(t)}{\partial \sigma_{mn}(t)}\frac{\partial \sigma_{mn}(t)}{\partial \sigma_{op}(\tau)}\varepsilon_{kl,t}\delta\varepsilon_{ij}dt \tag{28}$$

Thus, adjoint equation in incremental form with respect to the adjoint displacement $\bar{\boldsymbol{u}}$ is shown as:

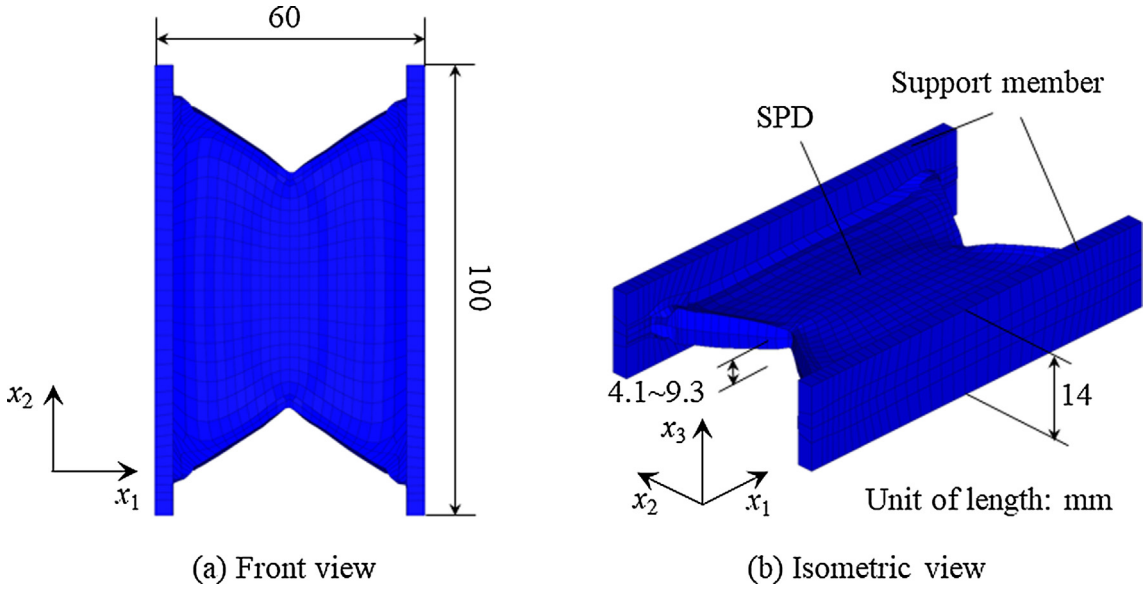

Fig. 16. Optimal shape of example 1 with thickness variation.

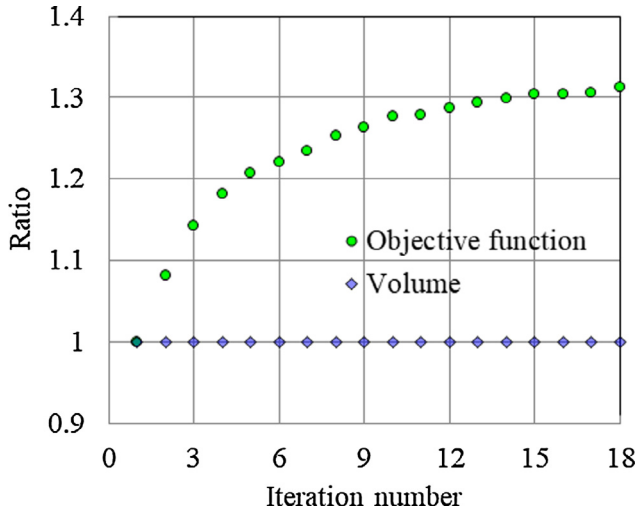

Fig. 17. Iteration history of example 1 with thickness variation.

$$\begin{aligned}\int_0^T a(\boldsymbol{u}'_{,t}(\tau), \bar{\boldsymbol{u}}(\tau)+\hat{\bar{\boldsymbol{u}}}(\tau))d\tau &= \int_0^T \int_{\Omega_s} C_{opqr}\varepsilon'_{qr,t}(\boldsymbol{u}_{,t})\{\bar{\varepsilon}_{op}(\bar{\boldsymbol{u}}) \\ &\quad + \hat{\bar{\varepsilon}}_{op}(\hat{\bar{\boldsymbol{u}}})\}dxd\tau \\ &= \int_0^T \{l(\boldsymbol{u}'_{,t}(\tau)) - l_h(\boldsymbol{u}'_{,t}(\tau))\}\}d\tau \\ &= \int_0^T (\int_{\Gamma_s} P_i u'_{i,t}d\Gamma - \int_{\Omega_s} C_{ijkl}h_{k,l}u'_{i,jt}dx)d\tau \\ &= -\int_T^0 (\int_{\Gamma_s} P_i u'_{i,t}d\Gamma \\ &\quad - \int_{\Omega_s} C_{ijkl}h_{k,l}u'_{i,jt}dx)d\tau, \quad \forall\, \boldsymbol{u} \in U\end{aligned} \tag{29}$$

According to the adjoint equation, the final adjoint displacement $\bar{\boldsymbol{u}}(T)$ caused by the adjoint load can be determined using the stiffness tensor at the final time T. Then, we can trace the adjoint displacement $\bar{\boldsymbol{u}}(\tau)$ from $\bar{\boldsymbol{u}}(T)$ to $\bar{\boldsymbol{u}}(0)$.

However, because calculation of the shape gradient function considering adjoint equation requires large memory capacity and high-speed computation, we carry out elastic-plastic analysis and adjoint analysis in the loading direction only at the points of designated time, and use the proportional loads among the points of designated time. As shown in Fig. 3, we draw the multi-step process of elastic-plastic analysis at first, in which we designate points N_1, N_2, N_3, … , N_n on the route of enforced displacements in $\sigma - \varepsilon$ curve from point O ($n = 200$ of each cycle is used in the present work), and determine Δt according to the precision and time of simulation. Next, we carry out adjoint analysis tracing from point N_n to point O, the final enforced displacement at point N_n is used for the calculation of adjoint strain in adjoint analysis. It needs to note that the stiffness tensor according to the optimal shape at each step used in adjoint analysis should be the same as that used in elastic-plastic analysis. To save the memory and time of computational simulation, the adjoint analysis is only carried out at the points N_1, N_2, N_3, … , N_n of designated time. Therefore, we calculate $\hat{\bar{\varepsilon}}_{op}(\hat{\bar{\boldsymbol{u}}}(\tau))$ at the points N_1, N_2, N_3, … , N_n by using Eq. (28) and substitute the results into Eq. (29) for obtaining the adjoint strain in terms of the shape gradient function.

3.4. Non-parametric shape optimization system for designing elastic-plastic SPDs under cyclic loading

The traction method for elastic 3D solid continua in terms of compliance minimization problem has been proposed in one of our previous works [39], in which its accuracy and effectiveness have been verified. In the present work, we extend the traction method to design elastic-plastic SPDs under cyclic loading. Because the traction method treats all nodes in the solid body as design variables and does not require any shape design parameterization, it is a non-parametric shape optimization method. The traction method is adopted in velocity analysis for determining the optimal design velocity field. It is also a gradient method with a Laplacian smoother [48]. In a common gradient-based shape optimization procedure, the shape gradient function (i.e. the sensitivity function) should be derived and calculated at first. Then, the determined shape gradient function is used for shape update. When the node coordinates are taken as design variables, the initial independent node movement technique, i.e. using the determined sensitivity function as the optimal design velocity field directly, often encounters extensive computation time, requiring re-mesh, and non-smooth optimal shape problems [49]. To solve these problems, we apply traction forces proportional to the negative shape gradient function $-\boldsymbol{G}$ in the normal direction to the design boundary of the objective structure (i.e. the SPDs in this study) in velocity analysis to determine the optimal design velocity field $\boldsymbol{V}$. This procedure is named as the traction method.

Fig. 4 shows the flowchart of the developed non-parametric shape optimization system for designing SPDs under cyclic loading. The system starts from elastic-plastic analysis (Eq. (20)) and adjoint analysis

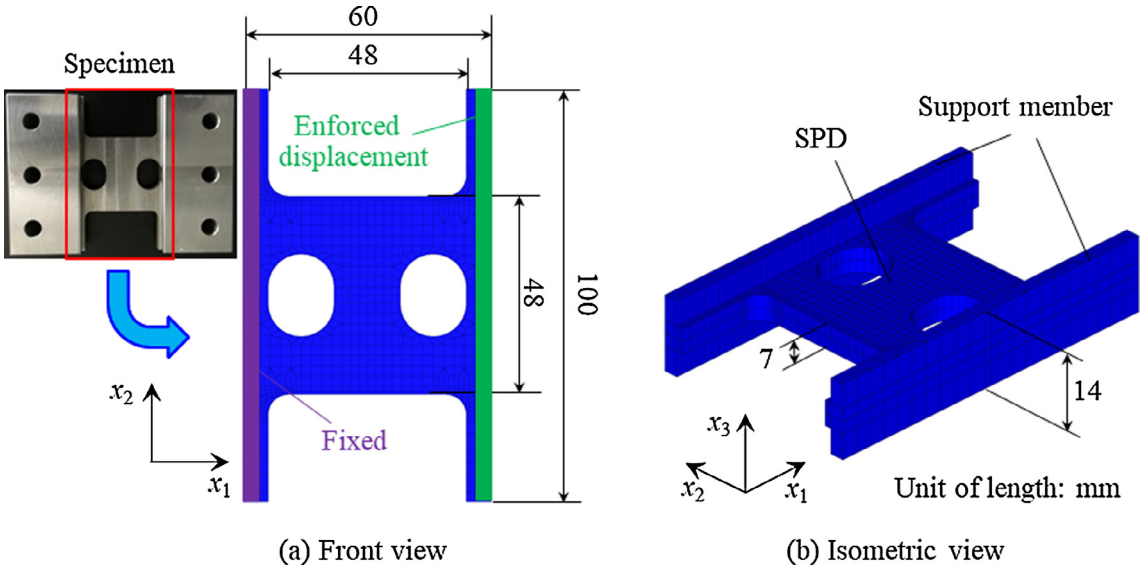

Fig. 18. Initial shape of example 2.

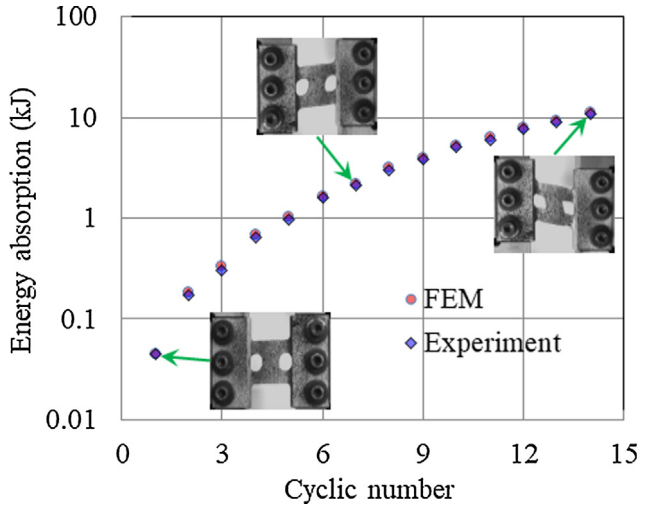

Fig. 19. Numerical vs. Experimental results of energy absorption of initial shape of Example 2.

(Eq. (29)), in which we perform the nonlinear finite element analysis of SPDs under cyclic loading to solve Eqs. (28) and (29). Then, substituting their outputs into Eq. (23), we calculate the shape gradient function $\boldsymbol{G}$. Next, we carry out velocity analysis by acting the traction forces proportional to the negative shape gradient function $-\boldsymbol{G}$ on the design boundary of the SPDs to get the optimal design velocity field $\boldsymbol{V}$ based on the traction method. At last, we update the shape of the SPDs according to $\boldsymbol{V}$. If the updated shape is not satisfied the volume constraint (Eq. (15)), we act a uniform traction forces on the design boundary of the SPDs to determine the Lagrange multiplier Λ for shape update again to satisfy the volume constraint. Repeating this process until the convergence is confirmed, we obtain the final optimal shape of SPDs under cyclic loading. In this process, elastic-plastic analysis and adjoint analysis are carried out using an implicit nonlinear FEM solver MSC NASTRAN, and velocity analysis is performed using a standard linear elastic FEM code.

4. Experimental verification

In terms of nonlinear numerical analysis of SPDs, some assumptions should be given. So it is preferred to verify nonlinear numerical analysis by experiments. Accordingly, we conducted cyclic loading test on SPDs using the Universal/Tensile Testing Machine (SHIMADU AG-250kN/300kNXplus) in the present work. The specimens of SPDs were made of LY100 steel, which is a kind of LYS. The constitutive law of LY100 determined from tensile coupon test with tensile speed 24 mm/min is shown in Fig. 5, which is also used in the numerical analysis. Moreover, the sizes of the specimens of SPDs and the cyclic loading conditions are the same as the FEM analysis given in each example.

We show the cyclic loading test setup in Fig. 6(a), in which two specimens of SPDs were set up between the self-made middle and side jigs. Fig. 6(b) shows the CAD drawing of the self-made jigs, in which the specimen of SPD was connected to the jigs by six M10 bolts. The middle jig was connected to the crosshead for producing the enforced displacements according to the tension and compression testing. Repeating the tension and compression testing by using the universal testing machine to perform the cyclic loading test could not only realize the simple shear loading, but also eliminate the bending force to the testing machine. The enforced displacement history of the cyclic loading test is shown in Fig. 7, in which the enforced displacement in each cycle was set as $\pm$ 1.8 mm, $\pm$ 3.6 mm, … , $\pm$ 12.6 mm (with increment $\pm$ 1.8 mm) and returned back to 0.0 mm at step 15. The loading speed is set as the same as the tensile coupon test (24 mm/min) for using the same constitutive law (Fig. 5) in experimental verification. The amount of the energy absorption of each step was determined by integrating the product of the reaction force vector.

Note here that, due to the limitation of the experimental facility, the enforced displacement history of the cyclic loading test (Fig. 7) and the model size of each design example are set only for experimental verification and evaluation of the developed optimization method. In a real structural design (e.g., design of dampers in bridge structures), the enforced displacement and the damper size should be larger than the given design examples. However, the enforced displacement and the damper size can be amplified by any times (e.g. 10 times) as much as each example in the finite element analysis. Thereby, if using the proposed dampers in the present work in a real structural design, for instance, when the enforced displacement is set as 10 times as much as shown in Fig. 7, the damper size in each design example can be also amplified by 10 times.

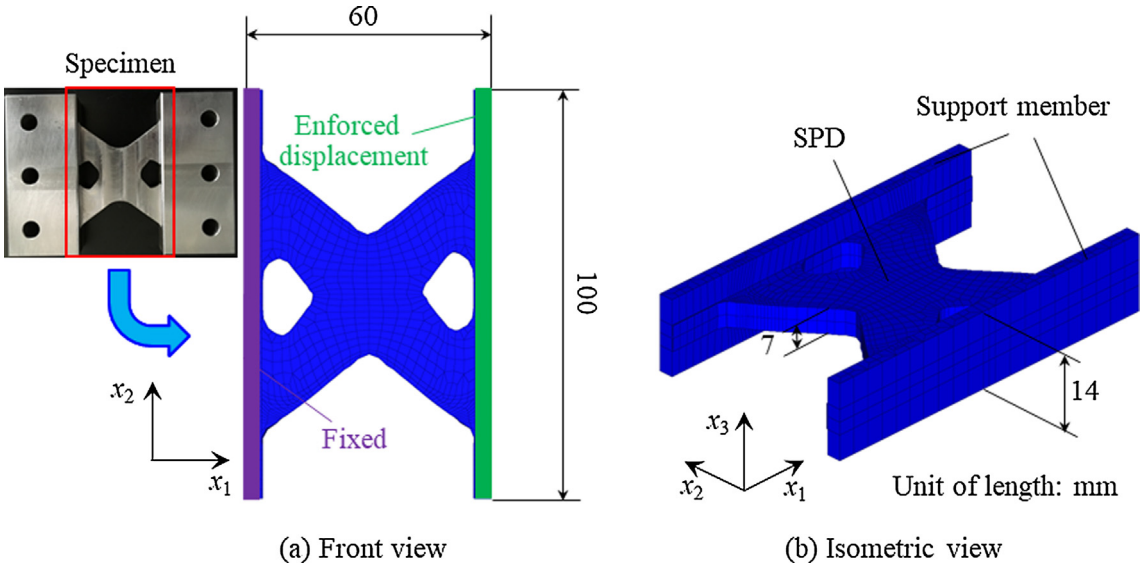

Fig. 20. Optimal shape of example 2 without thickness variation.

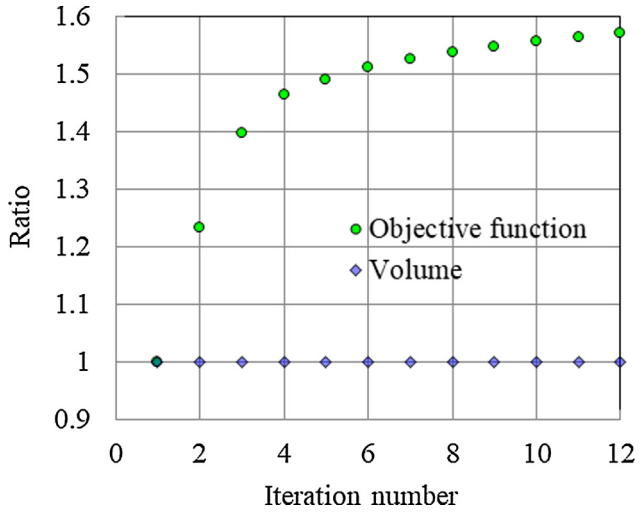

Fig. 21. Iteration history of example 2 without thickness variation.

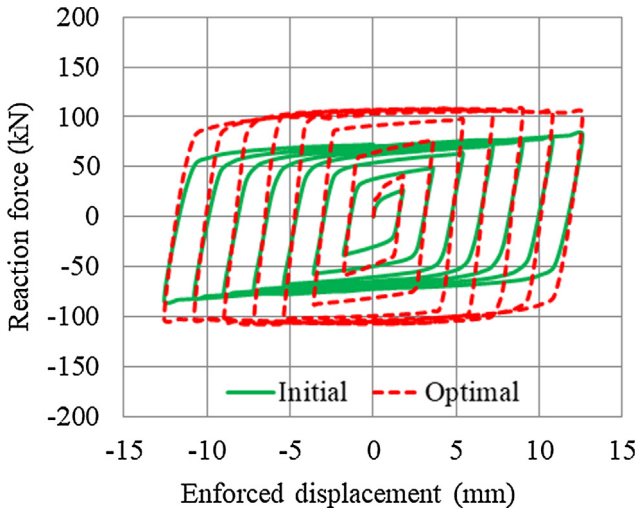

Fig. 22. Comparison of reaction force-enforced displacement curves of initial shape and optimal shape of example 2 without thickness variation.

5. Results and discussion

5.1. Initial setting of design examples

To confirm the validity of the developed shape optimization method, we design two examples for shape optimization of SPDs made of LY100 steel without or with holes. Because the shape optimization method is developed for 3D solid continua, we design the optimal shapes of SPDs without or with considering thickness variation in each example. In the finite element analysis, the hardening rule is defined by the Chaboche formulation [50]; ν is set as 0.3; one side of each SPD is fixed and cyclic enforced displacements acted on the other side of each SPD are used for simulating cyclic loading and evaluating the capacity of energy absorption; the constraint volume M_0 is set as the same as the initial volume.

5.2. Design example 1

In the first example, we optimize the shape a SPD without holes. The initial size of the SPD is shown as Fig. 8, in which (a) and (b) express the front view and isometric view of the initial shape, respectively. We also show the photo of the specimen used in the cyclic loading test in Fig. 8(a). The FEM model for elastic-plastic analysis and velocity analysis contains 2529 nodes and 1448 elements. In elastic-plastic analysis shown as Fig. 8(a), the left side of the SPD is fixed, and the right side is acted by the cyclic enforced displacements given as Fig. 7. In velocity analysis for shape update, all of the nodes on the two support members are constrained in x_1, x_2, and x_3 direction for maintaining the SPD edges connected to the support members. In the case of without considering thickness variation, all of the nodes on the SPD are constrained in x_3 direction in velocity analysis to keep the thickness of the SPD without variation. Because the plastic strain is also an evaluation criterion of LCF, we show the contour maps of plastic strain distribution determined from FEM at each load step of the initial shape in Fig. 9. The cyclic loading test of the specimen was performed to measure the energy absorption. Fig. 10 shows the comparison of the results of the energy absorption obtained from FEM and experiment, where the energy absorption of FEM is a little higher than that of experiment in most of the cyclic step. We consider the reason as that slight variation in x_3 direction occurred in the four corners of the SPD during the cyclic loading test, and hereby the capacity of energy absorption of the SPD was decreased. We also show the photos on the spot of the initial SPD at load steps 1, 7 and, 14 during the cyclic loading test in Fig. 10.

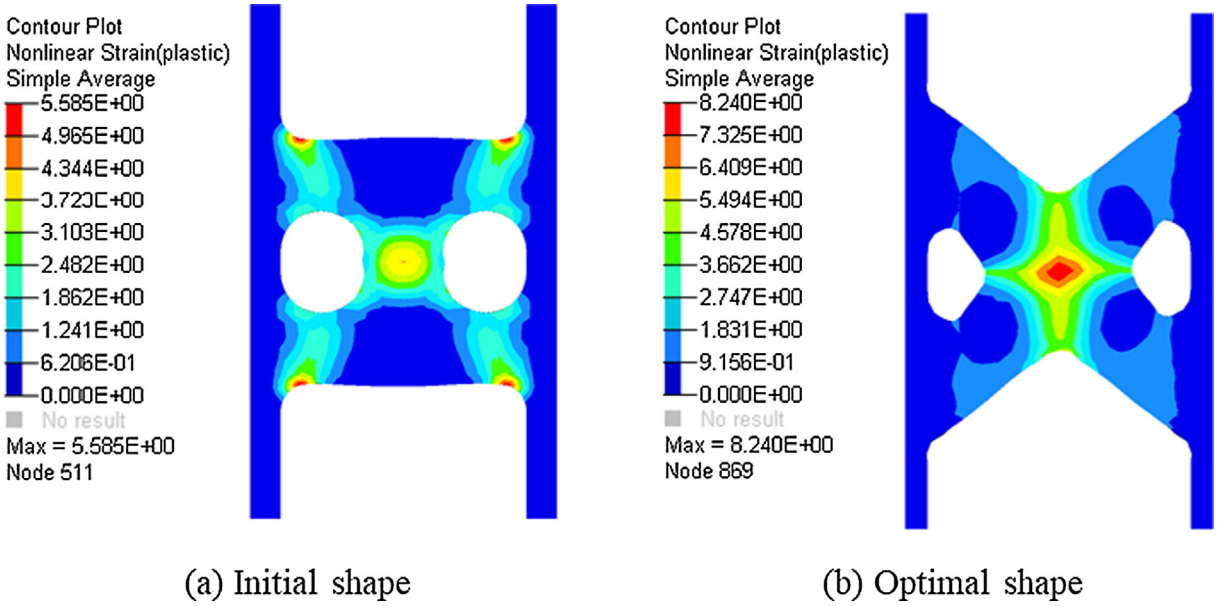

Fig. 23. Contour maps of plastic strain distribution in the SPDs of example 2 at the last cyclic step.

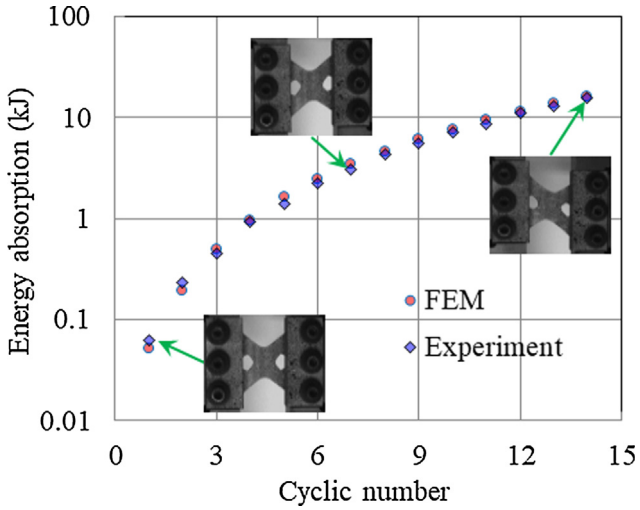

Fig. 24. Numerical vs. Experimental results of energy absorption of optimal shape of Example 2 without thickness variation.

Using the non-parametric shape optimization system introduced in Section 3.4, we design the optimal shape of the SPD without considering thickness variation shown as Fig. 11 at first. Fig. 11(a) shows the front view of the optimal shape of the specimen and the FEM model. In the optimal shape, the right and left sides of the SPD connected to the support members extend, whereas the middle part of the SPD shrinks. Fig. 11(b) shows the isometric view of the optimal FEM model, in which we can see that the thickness of the SPD is maintained as the same as the initial model without any variation. We show the iteration history of the shape design optimization of the SPD in Fig. 12, in which the objective function W is enhanced by 19% normalized to the initial shape under the volume constraint. To confirm this enhancement, the comparison of reaction force-enforced displacement curves of initial shape and optimal shape is shown in Fig. 13. The gross area (i.e. energy absorption) of the optimal shape is obviously larger than that of the initial shape, which can verify the validity and the effectiveness of the developed shape optimization method. We compare the contour maps of plastic strain distribution in the last load step of the initial shape and the optimal shape in Fig. 14. In the initial shape shown in Fig. 14(a), the plastic strain concentrates on the four corners of the SPD and reaches to a maximum value of 4.79, whereas the plastic strain concentrates on the center part of the SPD and becomes moderate owning a maximum value of 6.24 in the optimal shape as shown in Fig. 14(b). We also performed the cyclic loading test of the specimen of the optimal SPD. The comparison of the results of the energy absorption obtained from FEM and experiment is shown in Fig. 15, in which the energy absorption of FEM is also a little higher than that of experiment in most of the cyclic step because of the same reason illustrated above. Fig. 15 also shows the photos on the spot of the optimal SPD at steps 1, 7 and, 14 during the cyclic loading test.

One of the advantages of the developed shape optimization method of SPDs is that this method can also design SPDs in the thickness direction. In the case of with considering thickness variation during the shape design optimization, the boundary conditions of elastic-plastic analysis and velocity analysis are almost the same as the case of without considering the thickness, but all of the nodes on the SPD are free in x_3 direction in velocity analysis. We show the front view and the isometric view of the optimal FEM model with considering thickness variation in Fig. 16, in which we can see that the thickness of the SPD (initial thickness 7 mm) is also optimized between 4.1 mm and 9.3 mm. The iteration history of the shape design optimization of the SPD with considering thickness variation is shown in Fig. 17, in which the objective function W is enhanced by 31% normalized to the initial shape while satisfying the volume constraint. Hence, the optimal shape with considering thickness variation is more effective to resist cyclic loading than that without considering thickness variation (enhanced by 18%).

5.3. Design example 2

In the designing of SPDs, defects (e.g. holes) on SPDs are usually considered to meet some functional designs. For this reason, we design a SPD with holes by using the developed shape optimization method in the second example. Fig. 18(a) and (b) show the front view and isometric view of the initial shape of the SPD, respectively. In this example, two holes are set on the initial shape that with the same size of example 1. The FEM model for elastic-plastic analysis and velocity analysis contains 3127 nodes and 1840 elements. The boundary conditions of elastic-plastic analysis and velocity analysis of this example are totally the same as that of example 1. We also performed the cyclic loading test to measure the energy absorption in this example. The photo of the specimen of the initial shape of the SPD is shown in

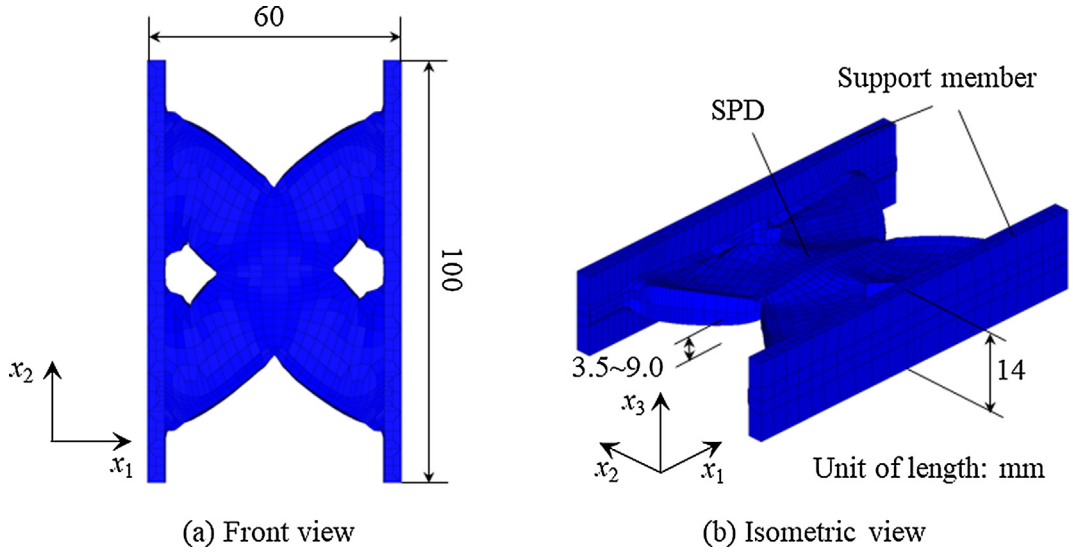

Fig. 25. Optimal shape of example 2 with thickness variation.

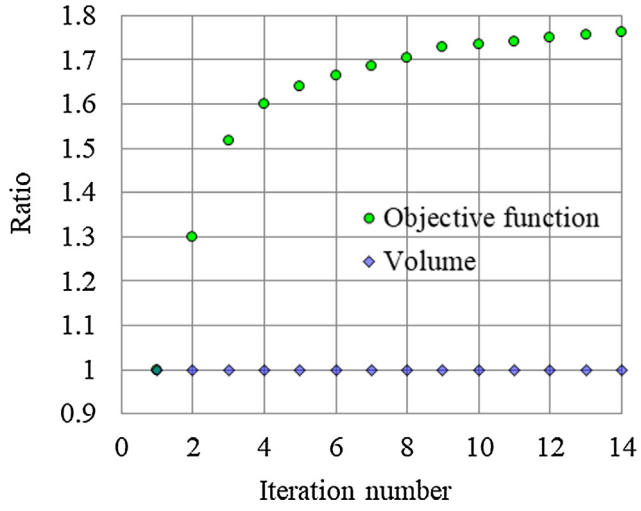

Fig. 26. Iteration history of example 2 with thickness variation.

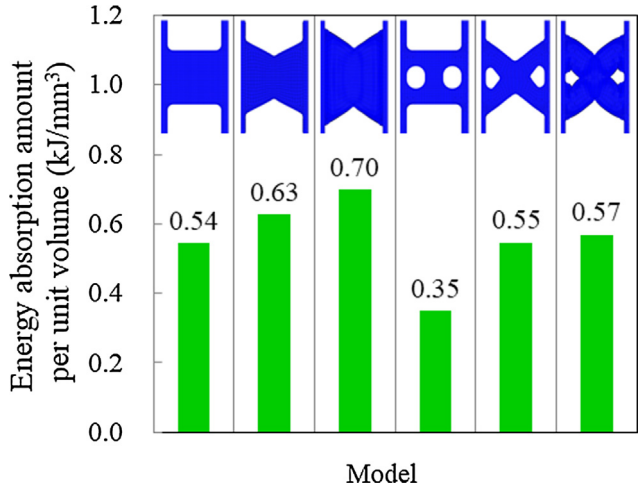

Fig. 27. Comparison of the energy absorption amount per unit volume of the numerical models of SPDs in Examples 1 and 2.

Fig. 18(a). The comparison of the results of the energy absorption obtained from FEM and experiment of the initial shape is shown in Fig. 19, in which the results match each other very well. We also present the photos on the spot of the initial SPD with two holes at steps 1, 7 and, 14 during the cyclic loading test in Fig. 19.

In the case of without considering thickness variation, we carry out shape design optimization of the SPD and show the optimal shape in Fig. 20. From the front view of the optimal shape shown in Fig. 20(a), the right and left sides connected to the support members of the optimal SPD extend and the middle part of the SPD shrinks. From the isometric view of the optimal shape shown in Fig. 20(b), the thickness of the SPD does not change and maintains 7 mm as the same as the initial model. The iteration history of this shape design optimization is shown in Fig. 21, in which the objective function W is enhanced by 57% normalized to the initial shape while satisfying the volume constraint. Fig. 22 shows the comparison of reaction force-enforced displacement curves of initial shape and optimal shape, where the gross area (i.e. energy absorption) of the optimal shape is obviously larger than that of the initial shape. To confirm the advanced plastic behavior of the optimal shape, the contour maps of plastic strain distribution in the last load step of the initial shape and the optimal shape are shown in Fig. 23. The maximum value of the plastic strain increases from 5.59 (initial shape) to 8.24 (optimal shape). We performed the cyclic loading test of the specimen shown as Fig. 20(a). The comparison of the results of the energy absorption obtained from FEM and experiment is shown in Fig. 24, where the results match each other very well in most of the cyclic step. Fig. 24 also shows the photos on the spot of the optimal SPD with two holes at steps 1, 7 and, 14 during the cyclic loading test.

Considering the thickness variation, we design the SPD shown in Fig. 18 by using the developed non-parametric shape optimization method. In this case, the boundary conditions of elastic-plastic analysis and velocity analysis are almost the same as the case of without considering the thickness, except for that all of the nodes on the SPD are free in x_3 direction in velocity analysis. The front view and the isometric view of the optimal FEM model of the SPD with considering thickness variation are shown in Fig. 25(a) and (b), respectively. The thickness of the SPD (initial thickness 7 mm) is optimized between 3.5 mm and 9.0 mm. From the iteration history shown in Fig. 26, the objective function W is enhanced by 76% normalized to the initial shape, which is more effective than optimizing the SPD without considering thickness variation. Thus, the developed shape optimization method shows an advantage of designing SPDs with considering thickness variation.

At last, we compare the energy absorption amount per unit volume

of the six numerical models of SPDs (Figs. 8, 11, 16, 18, 20, and 25) determined from FEM in Examples 1 and 2, and shown the comparison results in Fig. 27. The SPDs without holes owns higher energy absorption amount per unit volume in the initial model, the optimal model without considering thickness variation, and the optimal model considering thickness variation. In each example of SPDs without or with holes, the optimal models considering thickness variation shows the highest LCF behavior. Thus, the developed shape optimization process for solid continua under cyclic loading shows an advantage of design in the thickness direction of SPDs.

6. Conclusions

In summary, we developed a non-parametric shape optimization method for designing SPDs involving cyclic loading to enhance their LCF behavior and performed cyclic loading test for experimental verification. We considered the geometric and material nonlinearities, and employed the plastic work in terms of the Mises stress as the objective function in the present work. Shape gradient function was theoretically derived based on the Lagrange multiplier method, the material derivative formula, and the adjoint analysis. After velocity analysis, shape update was carried out based on the traction method under the volume constraint. We design two examples of SPDs without and with holes to confirm the validity and effectiveness of the developed shape optimization method. The results show that the objective function of optimal shape in each example was enhanced from 18% to 76%. We also performed cyclic loading test to verify the numerical analysis of the initial and optimal shapes. According to the comparison, the FEM and experimental results of energy absorption match each other very well in most of the cyclic step. Moreover, in each example, we executed two cases of shape design optimization of SPDs without/with considering thickness variation and concluded that the developed shape optimization method can design a SPD more effectively to resist cyclic loading with considering thickness variation. At last, we need to point out that the shape optimization method developed in the present work is not only used to design SPDs, but also can be applied in designing other nonlinear solid continua considering large deformation.

Acknowledgements

This work is supported by a grant-in-aid from the Research Center of Smart and Tough Machines at the Toyota Technological Institute.

References

[1] Soong TT, Spencer Jr. BF. Supplemental energy dissipation: state-of-the-art and state-of-thepractice. Eng Struct 2002;24:243–59.
[2] Ge H, Chen X, Matsui N. Seismic demand on shear panel dampers installed in steel-framed bridge pier structures. J Earthq Eng 2011;15:339–61.
[3] Michael DS, Michael CC. Semi-active control systems for seismic protection of structures: a state-of-the-art review. Eng Struct 1999;21:469–87.
[4] De Matteis G, Landolfo R, Mazzolani FM. Seismic response of MR steel frames with low-yield steel shear panels. Eng Struct 2003;25:155–68.
[5] Chan RWK, Albermani F, Williams MS. Evaluation of yielding shear panel device for passive energy dissipation. J Constr Steel Res 2009;65:260–8.
[6] Uang CM. An evaluation of two-level seismic design procedure. Earthq Spect 1993;9:121–35.
[7] Nakashima M, Iwai S, Iwata M, Takeuchi T, Konomi S, Akazawa T, et al. Energy dissipation behaviours of shear panels made of low yield steel. Earthq Eng Struct D 1994;23:1299–313.
[8] Zhang C, Zhang Z, Shi J. Development of high deformation capacity low yield strength steel shear panel damper. J Constr Steel Res 2012;75:116–30.
[9] Zhang C, Zhang Z, Zhang Q. Static and dynamic cyclic performance of a low-yield-strength steel shear panel damper. J Constr Steel Res 2012;79:195–203.
[10] Lee CH, Ju YK, Min JK, Lho SH, Kim SD. Non-uniform steel strip dampers subjected to cyclic loadings. Eng Struct 2015;99:192–204.
[11] Zhang C, Wei Y, Wang L, Wu M. Hysteretic mechanical property of low-yield strength shear panel dampers in ultra-large plastic strain. Eng Struct 2017;148:11–22.
[12] Liu Y, Shimoda M. Shape optimization of shear panel damper for improving the deformation ability under cyclic loading. Struct Multidisc Optim 2013;48:427–35.
[13] Taylor LM, Becker EB. Some computational aspects of large deformation, rate-dependent plasticity problems. Comput Meth Appl Mech Eng 1983;41:251–77.
[14] Hibbitt HD, Marcal PV, Rice JR. A finite element formulation for problems of large strain and large displacement. Int J Solids Struct 1970;6:1069–86.
[15] Döring R, Hoffmeyer J, Seeger T, Vormwald M. A plasticity model for calculating stress–strain sequences under multiaxial nonproportional cyclic loading. Comput Mater Sci 2003;28:587–96.
[16] Madsen LPB, Thambiratnam DP, Perera NJ. Seismic response of building structures with dampers in shear walls. Comput Struct 2003;81:239–53.
[17] Hossain MR, Ashra M, Albermani F. Numerical modelling of yielding shear panel device for passive energy dissipation. Thin Wall Struct 2011;49:1032–44.
[18] Usami T, Wang CL, Funayama J. Developing high-performance aluminum alloy buckling-restrained braces based on series of low-cycle fatigue tests. Earthq Eng Struct D 2012;41:643–61.
[19] Wang CL, Usami T, Funayama J, Imase F. Low-cycle fatigue testing of extruded aluminium alloy buckling-restrained braces. Eng Struct 2013;46:294–301.
[20] Ali A, Kim D, Cho SG. Modeling of nonlinear cyclic load behavior of I-shaped composite steel-concrete shear walls of nuclear power plants. Nucl Eng Technol 2013;45:89–98.
[21] Hejazi F, Toloue I, Jaafar MS. Optimization of earthquake energy dissipation system by genetic algorithm. Comput Aided Civ Inf 2013;28:796–810.
[22] Hu Z, Lu W, Thouless MD, Barber JR. Effect of plastic deformation on the evolution of wear and local stress fields in fretting. Int J Solids Struct 2016;82:1–8.
[23] Ihara H, Azegami H, Shimoda M. Shape optimization for displacement path control problem considering geometrical non-linearity. Trans Jpn Soc Mech Eng Ser A 2001;67(656):611–7. (in Japanese).
[24] Kosaka S, Shimoda M, Shi JX. Reaction forces control design of shell structures in plastic range based on free-form optimization method. Thin Wall Struct 2017;117:211–23.
[25] Featherston CA, Watson A. Buckling of optimised curved composite panels under shear and in-plane bending. Compos Sci Technol 2006;66:2878–94.
[26] Sonmez FO. Shape optimization of 2D structures using simulated annealing. Comput Meth Appl Mech Engrg 2007;196:3279–99.
[27] Ammar A, Huerta A, Chinesta F, Cueto E, Leygue A. Parametric solutions involving geometry: a step towards efficient shape optimization. Comput Meth Appl Mech Eng 2014;268:178–93.
[28] Deng K, Pan P, Su Y, Xue Y. Shape optimization of U-shaped damper for improving its bi-directional performance under cyclic loading. Eng Struct 2015;93:23–7.
[29] Deng K, Pan P, Sun J, Liu J, Xue Y. Shape optimization design of steel shear panel dampers. J Constr Steel Res 2014;99:187–93.
[30] Zhu B, Wang T, Zhang L. Quasi-static test of assembled steel shear panel dampers with optimized shapes. Eng Struct 2018;172:346–57.
[31] Meske R, Lauber B, Schnack E. A new optimality criteria method for shape optimization of natural frequency problems. Struct Multidisc Optim 2006;31:295–310.
[32] Le C, Bruns T, Tortorelli D. A gradient-based, parameter-free approach to shape optimization. Comput Meth Appl Mech Eng 2011;200:985–96.
[33] Stavropoulou E, Hojjat M, Bletzinger KU. In-plane mesh regularization for node-based shape optimization problems. Comput Meth Appl Mech Eng 2014;275:39–54.
[34] Hojjat M, Stavropoulou E, Bletzinger KU. The Vertex Morphing method for node-based shape optimization. Comput Meth Appl Mech Eng 2014;268:494–513.
[35] Riehl S, Friederich J, Scherer M, Meske R, Steinmann P. On the discrete variant of the traction method in parameter-free shape optimization. Comput Meth Appl Mech Eng 2014;278:119–44.
[36] Riehl S, Steinmann P. An integrated approach to shape optimization and mesh adaptivity based on material residual forces. Comput Meth Appl Mech Eng 2014;278:640–63.
[37] Azegami H. Solution to domain optimization problems. Trans Jpn Soc Mech Eng Ser A 1994;60(574):1479–86. (in Japanese).
[38] Azegami H, Takeuchi K. A smoothing method for shape optimization: traction method using the Robin condition. Int J Comp Meth-Sing 2006;3(1):21–33.
[39] Shi JX, Shimoda M. Interface shape optimization of designing functionally graded sandwich structures. Compos Struct 2015;125:88–95.
[40] Shi JX, Shimoda M. Free-form optimization of sandwich structures for controlling thermal displacement. Compos Struct 2016;148:39–49.
[41] Rohan E, Whiteman JR. Shape optimization of elasto-plastic structures and continua. Comput Meth Appl Mech Eng 2000;187:261–88.
[42] Ihara H, Azegami H, Shimoda M, Watanabe K. Solution to shape optimization problem considering material non-linearity. Trans Jpn Soc Mech Eng Ser A 2000;66(646):1111–8. (in Japanese).
[43] Wang W, Clausen PM, Bletzinger KU. Improved semi-analytical sensitivity analysis using a secant stiffness matrix for geometric nonlinear shape optimization. Comput Struct 2015;148:143–51.
[44] Kahrobaiyan MH, Rahaeifard M, Ahmadian MT. A size-dependent yield criterion. Int J Eng Sci 2014;74:151–61.
[45] Madenci E, Oterkus S. Ordinary state-based peridynamics for plastic deformation according to von Mises yield criteria with isotropic hardening. J Mech Phys Solids 2016;86:192–219.
[46] Rokhgireh H, Nayebi A, Chaboche JL. Application of a new distortional yield surface model in cyclic uniaxial and multiaxial loading. Int J Solids Struct 2017;110:219–38.
[47] Choi KK, Kim NH. Structural sensitivity analysis and optimization 1 Linear systems. New York: Springer; 2005.
[48] Shimoda M, Liu Y. A non-parametric free-form optimization method for shell structures. Struct Multidisc Optim 2014;50:409–23.
[49] Braibant V, Fleury C. Shape optimal design using B-splines. Comput Meth Appl Mech Eng 1984;44:247–67.
[50] Chaboche JL. Constitutive equations for cyclic plasticity and cyclic viscoplasticity. Int J Plasticity 1989;5:247–302.